

ARTICLE OPEN



The underappreciated role of anthropogenic sources in atmospheric soluble iron flux to the Southern Ocean

Mingxu Liu¹✉, Hitoshi Matsui¹✉, Douglas S. Hamilton², Kara D. Lamb^{3,4}, Sagar D. Rathod⁵, Joshua P. Schwarz⁴ and Natalie M. Mahowald²

The atmospheric deposition of soluble (bioaccessible) iron enhances ocean primary productivity and subsequent atmospheric CO₂ sequestration in iron-limited ocean basins, especially the Southern Ocean. While anthropogenic sources have been recently suggested to be important in some northern hemisphere oceans, the role in the Southern Ocean remains ambiguous. By comparing multiple model simulations with the new aircraft observations for anthropogenic iron, we show that anthropogenic soluble iron deposition flux to the Southern Ocean could be underestimated by more than a factor of ten in previous modeling estimates. Our improved estimate for the anthropogenic iron budget enhances its contribution on the soluble iron deposition in the Southern Ocean from about 10% to 60%, implying a dominant role of anthropogenic sources. We predict that anthropogenic soluble iron deposition in the Southern Ocean is reduced substantially (30–90%) by the year 2100, and plays a major role in the future evolution of atmospheric soluble iron inputs to the Southern Ocean.

npj Climate and Atmospheric Science (2022)5:28; <https://doi.org/10.1038/s41612-022-00250-w>

INTRODUCTION

Iron is a crucial micronutrient limiting primary production in many marine basins^{1–4}. Atmospheric deposition to the open oceans is a major source of new soluble iron, commonly used as a proxy for iron that is bioavailable for ocean biota uptake. By changing marine phytoplankton growth, atmospheric iron deposition modulates ocean-atmosphere carbon dioxide (CO₂) exchange rates and sequesters CO₂ to the deep ocean^{5–7}. The prevailing view that the global atmospheric soluble iron supply is predominantly associated with natural dust emissions is evolving given, the growing body of evidence showing that pyrogenic iron from anthropogenic combustion (AN) and biomass burning (BB) sources are important contributors to soluble iron deposition to many open ocean regions because of their high fractional solubility^{8–12}.

The Southern Ocean, as the world's largest high-nutrient-low-chlorophyll (HNLC) region, plays an important role in controlling atmospheric CO₂ pressure and primary production there and is most likely iron-limited^{13–17}. Globally, the response of ocean biogeochemistry in this region may be one of the most sensitive to changes in the atmospheric iron deposition flux¹⁸. Atmospheric iron deposited here originates mainly from the Southern Hemisphere regions of Southern Africa, Australia, and South America. Each region supplies dust, BB, and AN iron although with different fractional contributions¹⁹. The individual contributions of these major sources to soluble iron deposition to the Southern Ocean remain an open question in part because of the limited observations in this remote region, though many studies believe that AN iron (mainly from fossil fuel combustion) contribution is minor (possibly less than 10%) in the Southern Ocean^{20–22}. Unlike iron from dust and BB, AN iron depends completely on human activities and thus varies significantly over time in response to resource demands and societal priorities. Understanding the anthropogenic contribution to soluble iron deposition is essential

for assessing both present and future responses of marine carbon sinks.

A recently developed aircraft measurement²³ dataset of anthropogenically sourced iron oxides (mainly in the form of magnetite) across the Pacific and Atlantic Oceans provides a new constraint on the AN iron supply to the Southern Ocean. We integrate this observational dataset with global aerosol modeling to improve the estimates of AN iron concentrations and deposition fluxes over the Southern Ocean (defined as ocean basins to the south of 30°S in this study). Magnetite nanoparticles in conjunction with other iron-bearing minerals of anthropogenic origin are produced by a wide range of human activities including fossil fuel combustion and iron smelting; hence in this work magnetite is used as a proxy to evaluate anthropogenic iron budgets in the atmosphere against the observations²⁴. We use an updated anthropogenic emission inventory for iron minerals²⁵ to model the AN iron atmospheric budget in a control simulation (hereafter, CTRL), as well as a commonly used AN iron inventory developed by Luo et al.²⁶ (hereafter, Luo2008) for comparison. Our results suggest that anthropogenic iron is much more important than traditionally thought for present-day soluble iron deposition in the Southern Ocean and for future changes owing to projected reductions in anthropogenic emissions. This study has potential to advance the understanding of the ocean biogeochemical responses in the Earth system to changing human activities.

RESULTS

Observational constraints on the anthropogenic iron budget in the atmosphere

Iron as magnetite accounts for about 70% of global total AN iron emissions in the recently-developed anthropogenic iron emission inventory (Supplementary Fig. 1)²⁵. In addition to AN sources, observed magnetite particles in the atmosphere also originates

¹Graduate School of Environmental Studies, Nagoya University, Nagoya, Japan. ²Department of Earth and Atmospheric Science, Cornell University, Ithaca, NY, USA. ³Cooperative Institute for Research in the Environmental Sciences, University of Colorado, Boulder, CO, USA. ⁴Chemical Sciences Division, NOAA Earth System Research Laboratory, Boulder, CO, USA. ⁵Department of Atmospheric Science, Colorado State University, Fort Collins, CO, USA. ✉email: liu.mingxu@ambox.nagoya-u.ac.jp; matsui@nagoya-u.jp

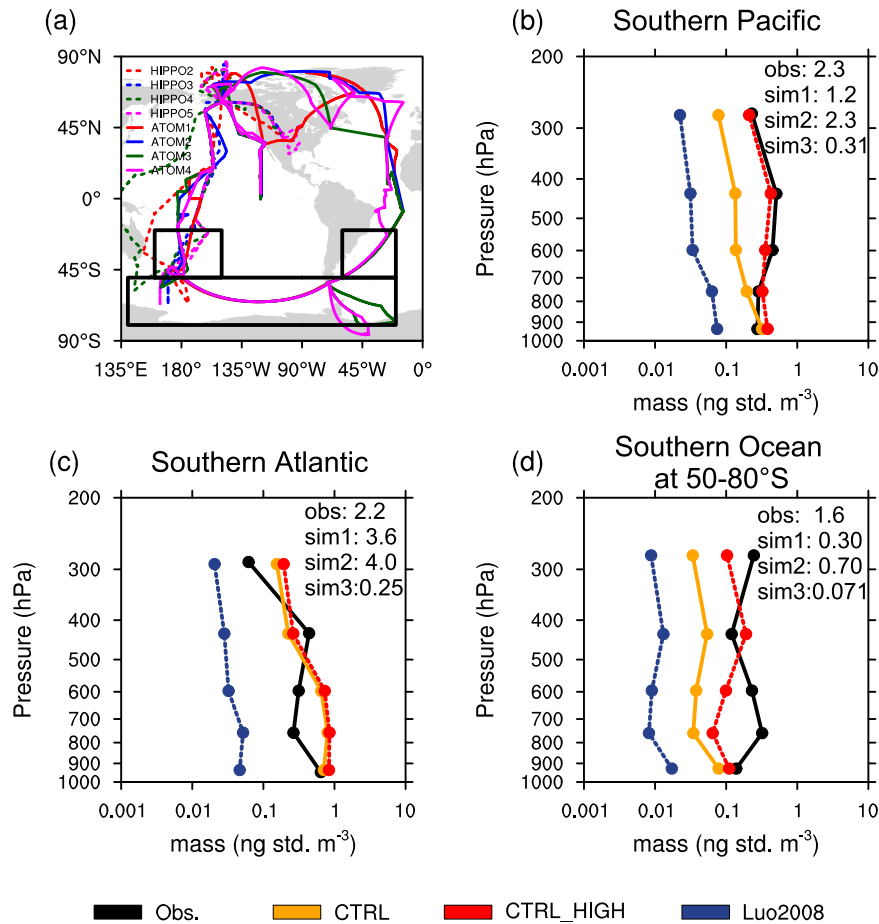


Fig. 1 Comparisons of magnetite concentration profiles. **a** Flight routes of eight series of aircraft campaigns during 2009–2018. **b–d** anthropogenic magnetite concentrations in observations and simulations over the Southern Pacific (20–50° S, 160° E–135° W), the Southern Atlantic (20–50° S, 20° W –60° W), and the high-latitude Southern Ocean basin (50–80° S, 140° E–20° W). The results of the CTRL (blue squares), the CTRL_HIGH (red squares), and the Luo2008 simulations are compared with the observation data. Both simulation and observation data were binned at intervals of around 160 hPa. Magnetite concentrations are shown at standard temperature and pressure (std.), 1,013 hPa and 0 °C. The column-integrated concentrations ($\mu\text{g m}^{-2}$) for both the observations (obs) and simulation results (sim1 = CTRL; sim2 = CTRL_HIGH; sim3 = Luo2008) are shown in the panels.

from mineral dust. The fraction of dust magnetite, however, has been excluded in the observations by classifying the aerosol populations into different sources (anthropogenic and mineral dust) on a single particle basis²³; thus the model-observation differences of magnetite particles in this study should be attributable only to anthropogenic sources. Here, we validate the modeled AN iron abundance in three oceanic regions encompassing both the middle and high latitudes of the Southern hemisphere, namely the Southern Pacific (20–50°S, 160°E–135°W), the Southern Atlantic (20–50°S, 20–60°W), and part of the high-latitude Southern Ocean (50–80°S, 140° E–20°W), by using the aircraft measurements of anthropogenic magnetite mass concentrations (Fig. 1). We compare magnetite concentration profiles along the flight routes in each region between the observations and the CTRL simulation. We find a good agreement between modeled and observed magnetite concentration profiles over the Southern Atlantic, although with an appreciable overestimation at low altitudes (pressure greater than 600 hPa) (Fig. 1c). Meanwhile, the CTRL simulation underestimates the magnetite concentrations by a factor of 5–10 in the middle and upper troposphere (≤ 400 hPa) over both the Southern Pacific and the high-latitude Southern Ocean (Fig. 1b, d). By contrast, a reasonable model-observation agreement has been achieved for black carbon concentrations with their discrepancies mostly less than a factor of 2 (Supplementary Fig. 2), and therefore the large biases of

simulated magnetite concentrations are most likely associated with the uncertainties embedded in the emission fluxes.

To address the underestimation of AN iron budgets over southern Pacific Oceans, we perform three sensitivity simulation experiments by separately imposing a factor-of-five enhancement of the AN iron emissions from each of the three major continental source regions (i.e., Southern Africa, Australia and surrounding countries, and South America; see Supplementary Fig. 3 for their locations). For the model-observation comparison in the high-latitude Southern Ocean, we find that the gaps can be reduced effectively by scaling upward the emissions from all source regions (Supplementary Fig. 3), suggesting the potential underestimation of AN iron emissions across the Southern Hemisphere. However, the enhancements of the emissions from Australia and South America would severely degrade the model performance over the Southern Pacific and the Southern Atlantic Oceans. Hence, it appears that scaling up the emissions in Southern Africa can achieve the best simulation of magnetite profiles (red dashed lines in Fig. 1) across the Southern Ocean basins, though we cannot rule out the possibility of the emission underestimation in another two continental regions. The assumed scaling factor (x5.0 in this study) is tunable and linked to the model-observation gaps of the magnetite mass budget across the Southern Hemisphere (shown in Fig. 1). In the following analysis, we regard the simulation result based on the enhanced AN iron emissions for

Southern Africa (hereafter, CTRL_HIGH) as the best case in modeling the AN iron abundance over the Southern Ocean.

Additionally, the use of AN iron emissions from the Luo2008 inventory²⁶ leads to notably worse results of the comparison with magnetite observations (Fig. 1), because AN iron emissions are much lower in the Luo2008 inventory than in the inventories used in CTRL and CTRL_HIGH. The Luo2008 simulation severely underestimates, by up to two orders of magnitude, AN iron oxide concentrations over the Southern Ocean, even when all modeled AN iron are assumed to be present as magnetite. As this inventory has been commonly applied in previous studies^{27,28}, the resulting estimates of anthropogenic contribution to total soluble iron deposition have been therefore underestimated. Our new observation constraints suggest that the role of anthropogenic sources in atmospheric iron inputs to the Southern Ocean should be revisited by using our improved AN iron emission inventory.

Contribution of anthropogenic sources to soluble iron deposition

We next estimate the atmospheric soluble iron deposition to the Southern Ocean from AN sources and evaluate its importance by comparing it with dust and BB contributions based on the present-day iron emissions from dust, BB, and AN sources (see Methods). Soluble iron deposition is the product of the source-specific iron deposition in our simulations and the corresponding fractional iron solubility estimated in a global aerosol model with a detailed iron processing (Supplementary Fig. 4)¹². The simulated iron solubility values show a reasonable agreement with available near-surface observations over global oceans (Supplementary Figs. 5–6).

Three different AN iron emission scenarios (i.e., CTRL, CTRL_HIGH, and Luo2008) are involved in the calculation of soluble iron deposition. We find that this range of AN iron emissions results in a wide range of both AN soluble iron fluxes and their fractional contributions to the total (the sum of dust, BB and AN) soluble iron deposition in the Southern Ocean (Fig. 2a). Compared to the CTRL simulation, the AN soluble iron deposition flux to the whole Southern Ocean is more than doubled, from 2.5 to 6.5 Gg Fe yr⁻¹, by the enhancement of AN iron emission in the Southern Hemisphere (CTRL_HIGH). In comparison, the Luo2008 simulates more than an order of magnitude lower flux at 0.53 Gg Fe yr⁻¹. Consequently, the total soluble iron deposition to the Southern Ocean varies by above a factor of 2 from 4.6 (Luo2008) to 10.6 Gg Fe yr⁻¹ (CTRL_HIGH). The AN iron fractional contributions to the total deposition flux are 38%, 61%, and 11% in CTRL, CTRL_HIGH, and Luo2008, respectively. The dominant contributor shifts from the BB iron in Luo2008 and CTRL to the AN iron in CTRL_HIGH. The dust soluble iron contribution (0.91 Gg Fe yr⁻¹) appears to be less important than either AN or BB iron owing to its much lower fractional solubility at deposition (1.5% averaged over the Southern Ocean), though mineral dust dominates the total iron deposition (the sum of soluble and insoluble iron) in the Southern Ocean.

The spatial-resolved AN contributions in the CTRL_HIGH case are enhanced by up to one order of magnitude across much of the Southern Ocean compared to the results in the Luo2008 case (Fig. 2). Our global modeling results reveal that the fractional contributions of AN sources to the total soluble iron deposition are pronounced in many ocean basins including the Southern Ocean. In the CTRL simulation, the AN sources contribute to about 50% of the soluble iron deposition in the oceanic regions around Southern Africa, Australia, and South America (Fig. 2b); further in the CTRL_HIGH simulation, the AN iron contributions are elevated in most of the Southern Ocean and reach up to 80% near Southern Africa (Fig. 2c). The strong Southern Hemisphere westerly winds (30–60°S) would enhance the effects of the emission enhancement in CTRL_HIGH on soluble iron deposition

by transporting iron emitted from Southern Africa long distances to remote Southern Ocean regions. The proportional area where AN iron is the largest source of soluble iron deposition in the Southern Ocean increases substantially from 34% (CTRL) to 87% (CTRL_HIGH). By contrast, in the Luo2008 simulation, the fractional contributions of AN sources to soluble iron deposition across the Southern Ocean are relatively minor, mostly within 0–20% (Fig. 2d).

The monthly AN deposition fluxes are elevated by a factor of 7–15 in the CTRL_HIGH case compared to those using the Luo2008 inventory, and consequently constitute much more fractions of the monthly accumulated soluble iron deposition to the Southern Ocean (Supplementary Fig. 7). While dust and BB activities have the season-dependent nature, AN sources in the CTRL_HIGH simulation provide relatively stable iron fluxes to the Southern Ocean with small seasonal perturbations, though the AN importance varies in different seasons due to seasonal fluctuations of dust and BB iron deposition. In CTRL_HIGH, the AN contributions are dominant in all seasons except in the local winter (August–September), when the BB contribution is the largest. This assessment of monthly AN iron contributions could improve understanding of the daily-to-monthly responses of ocean primary production to changes in iron availability by natural and human activities²⁹.

Future soluble iron deposition to the Southern Ocean

To understand the future evolution of soluble iron deposition fluxes to the Southern Ocean in response to potential changes in AN sources, we project future AN iron emissions (ca. 2100 CE) separately for CTRL, CTRL_HIGH, and Luo2008 cases according to the four Tier-1 shared socio-economic pathways (SSPs; see Methods). Dust and BB emissions are assumed to be unchanged relative to the present day. We also assume the fractional iron solubility for AN, BB and dust sources to be unchanged as the present-day data. The predicted percentage changes from the present day to the future in AN soluble iron deposition to the whole Southern Ocean are consistent among CTRL, CTRL_HIGH, and Luo2008, within –30 and –90%, for the applied SSP projections (SSP1–26, SSP2–45, SSP3–70, and SSP5–85). However, the percentage changes of the total deposition flux (sum of AN, dust, and BB) vary significantly (Fig. 3a); they are highest in CTRL_HIGH (ranging from –21% to –55% depending on the SSP scenarios) and lowest in Luo2008 (from –5% to –10%). The largest absolute decreases of the total soluble iron flux among the SSP scenarios in CTRL, CTRL_HIGH, and Luo2008 are 2.3, 5.9, and 0.46 Gg yr⁻¹, respectively. These results suggest that the future evolution of atmospheric soluble iron deposition varies with the AN iron emissions at present day. The CTRL_HIGH simulation results, which are supported by the aircraft observations, point to a nonnegligible or even major role of AN iron in future changes in atmospheric soluble iron inputs to the Southern Ocean.

We further examine the global distribution of the present-to-future changes for each of the three present-day anthropogenic emission inventories based on the SSP5 scenario, which represents the largest decrease of AN iron at the end of the Century (Fig. 3). At a global scale, the percentage changes in total soluble iron deposition fluxes to the Southern Ocean are closely associated with the spatial pattern of the present-day AN percent contributions (Fig. 2). In CTRL, changes are marked (< –30%) in continental outflows near Southern Africa, Australia, and South America, while in CTRL_HIGH, more than half of the Southern Ocean region show a 50% or larger decrease of total soluble iron deposition. Because the present-day AN contribution is much lower in the Luo2008 simulation, the modeled present-to-future changes in soluble iron deposition to the Southern Ocean are relatively small (around –10%). These results suggest that AN iron emissions are of great importance to impact the future

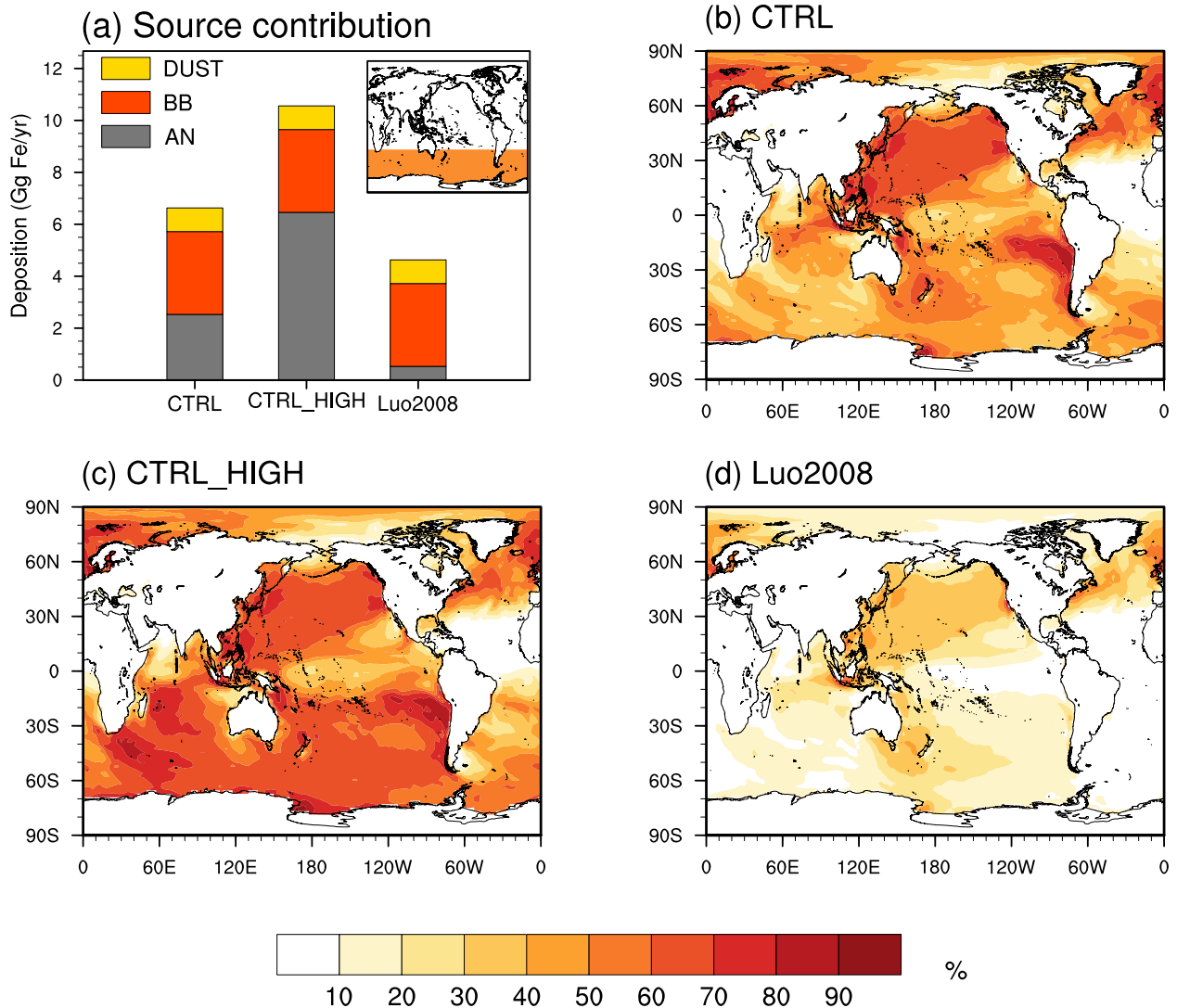


Fig. 2 Anthropogenic soluble iron deposition to the Southern Ocean. **a** Annual accumulated soluble iron deposition fluxes of AN (anthropogenic), BB (biomass burning), and dust iron over the Southern Ocean ($>30^{\circ}$ S; marked in the top right of Fig. 2a) in the CTRL, CTRL_HIGH, and Luo2008 simulations. **b–d** Global distribution of the percent contributions (%) of AN iron to the total soluble iron deposition in each simulation.

atmospheric soluble iron deposition to the Southern Ocean, where the sensitivity of ocean biogeochemistry to the atmospheric soluble iron supply is likely high¹⁸.

Future changes in atmospheric soluble iron deposition to the Southern Ocean rely on both the source contributions of iron from dust, BB, and AN in the present day and their respective changes from the present day to the future. The integration of observational constraints and the global aerosol modeling in this work points to an important contribution (probably as high as 60% based on the CTRL_HIGH simulation) of AN iron to total soluble iron deposition flux to the Southern Ocean in the present day. However, projections of future changes in both dust and BB emissions are highly uncertain owing to the complex factors that determine these emissions, including climate change, land use and land cover change, and human activities. The intensity of natural dust activity is expected to increase under a potentially warmer climate³⁰; thus, associated atmospheric dust iron fluxes to ocean basins might also increase. Estimates of the magnitude and sign of present-to-future changes in BB iron emissions also vary. In estimates based on Tier-1 SSP scenarios, the global BC emissions from open fires (as a proxy for BB iron) are projected to decrease

by 0.5–35% between 2015 and 2100³¹. Conversely, it has been suggested that fire emissions will increase by 2100 as a result of a warmer climate^{32,33}. Though only the future AN iron evolution is considered in this study, we infer that AN activities play a major role in future changes of soluble iron deposition to the Southern Ocean.

DISCUSSION

The identification of source contributions of dust, BB, and AN to the atmospheric bioavailable iron supply in the present-day climate is key for predicting ocean biogeochemical responses to future changes in soluble iron deposition. However, the scarce observations of the atmospheric component of the iron cycle have hindered our understanding of the major determinants of soluble iron deposition fluxes to the oceanic region. No modeling studies have provided a reliable representation of atmospheric iron three-dimensional distributions over the Southern Ocean until now. This study applies a new aircraft measurement data for AN iron oxides (excluding those from mineral dust) to constrain the model simulation of AN iron distributions over the Southern Ocean and

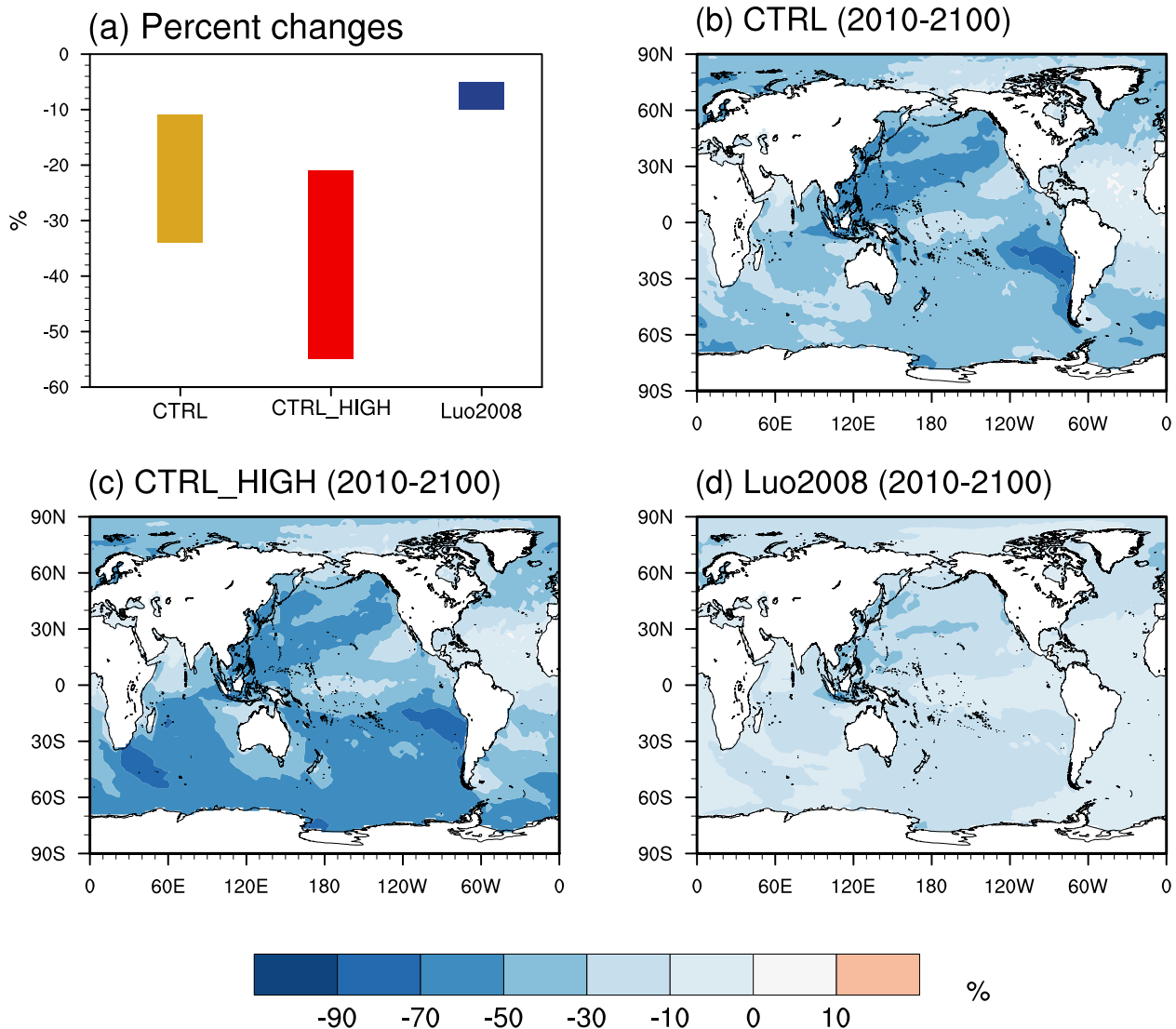


Fig. 3 Present-to-future changes in soluble iron deposition. **a** The predicted changes in total soluble iron deposition in the Southern Ocean (>30°S) from the present day (2010) to the future conditions (2100) in the CTRL, CTRL_HIGH, and Luo2008 simulations according to a suite of projections (SSPs) of future anthropogenic emissions (SSP1–26, SSP2–45, SSP3–70, and SSP5–85). **b–d** Global distribution of the percent changes predicted by each simulation using the SSP5–85 scenario, which represents the maximum percent changes of soluble iron deposition over the Southern Ocean as a whole.

consequently to reevaluate the AN iron contribution to the atmospheric soluble iron inputs to the ocean.

Our estimate with improved AN iron emission inventory (CTRL_HIGH) enhances the AN soluble iron deposition to the Southern Ocean by more than a factor of 10, which substantially elevates its share in atmospheric soluble iron. Based on our estimates of dust and BB irons, we show that AN iron accounts for approximately 60% of annual atmospheric soluble iron deposition directly to the Southern Ocean, compared to only 10% based on the previous AN inventories (Fig. 4). This fraction depends on the simulations of natural source (dust and BB) contributions, which varied substantially in existing estimates (Supplementary Note 1). If we follow some much higher contributions of iron from natural sources like Scanza et al.²⁸ and Hamilton et al.¹⁹ (see Supplementary Table 1), the resulting fractional contributions of AN iron from our improved estimate are still appreciable, showing approximately one third of the total soluble iron deposition. Moreover, unlike the season-dependent nature of dust and BB iron emissions, the monthly AN iron deposition fluxes are relatively stable throughout one year and potentially dominate the

atmospheric soluble iron inputs to the ocean basin in individual months from our estimate. Therefore, this study concludes that the role of atmospheric AN iron in the Southern Ocean should be revisited, as previous studies have been not validated with the observations for AN iron oxides and they always overlook its contribution on the atmospheric soluble iron inputs.

More observational constraints and improved representation of iron emissions and atmospheric processing in models are still required to better reproduce the atmospheric component of the global iron cycle, because the uncertainties, including the modeling of iron emission fluxes, size distributions of iron-bearing particles, and the fractional iron solubility, remain large due to the limitation of observations in space and time (as discussed in Supplementary Note 2). Note that many aerosol models with advanced iron processing modules cannot reproduce the observed near-surface high solubility (>10%) of iron in the Southern Ocean, implying some important missing sources^{9,34}. The increases of Southern Hemisphere AN iron emissions for better reproducing atmospheric AN iron vertical profiles have the potential to provide more highly soluble iron in the high-latitude

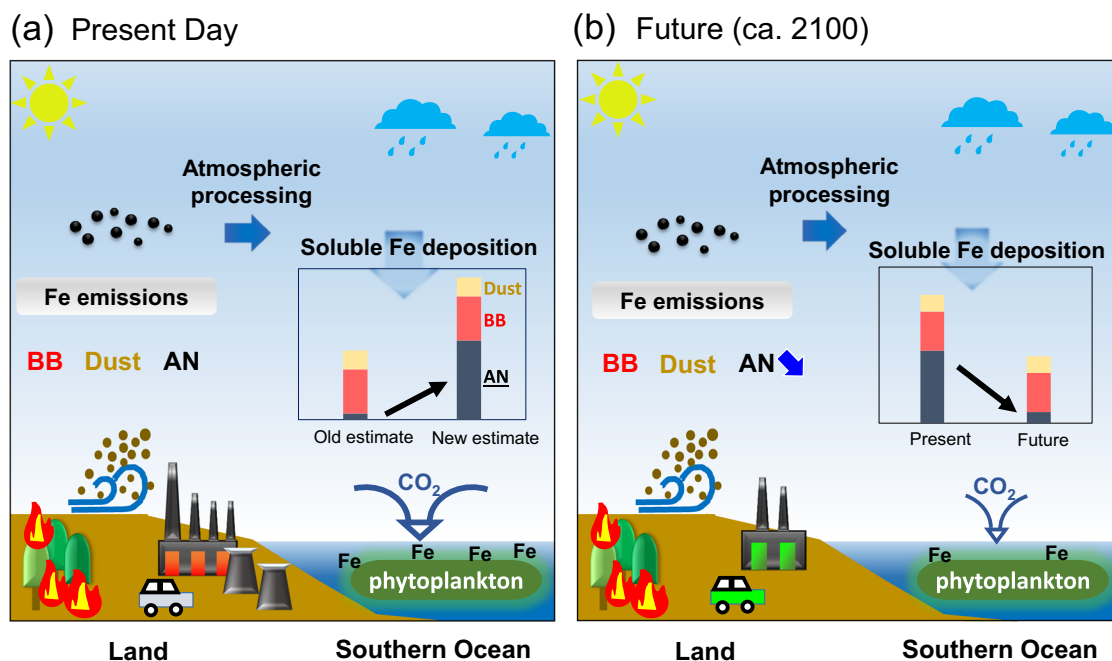


Fig. 4 Schematic of soluble iron deposition to the Southern Ocean. **a** The improved contribution of anthropogenic (AN) iron in the total soluble iron deposition in the present day. The simulation results are derived from the CTRL_HIGH case (i.e., new estimate of AN iron deposition in the Fig. 4a) and the Luo2008 case (old estimate of AN iron). **b** The present-to-future changes in soluble iron deposition. Iron emissions from biomass burning (BB) and dust sources are the same in the old and new estimates at the present-day conditions and are assumed to be stable from the present day to the future.

Southern Ocean. In addition, biomass burning, such as Australian wildfires, has also been recognized as a significant contributor to bioavailable iron and subsequent biological productivity in the Southern Ocean³⁵. A large quantity of field observations on iron chemistry over remote oceans are desirable to validate the iron cycle in models.

Our findings will facilitate more informed assessment of future responses of marine biogeochemistry and carbon sinks in the Southern Ocean. As an important source of the oceanic iron cycle, atmospheric supplies of new iron to the Southern Ocean are thought to vary substantially from the past to the future due to human activities, while other oceanic sources of iron, such as hydrothermal vents or sedimentary, may be relatively stable^{12,18,36}. AN iron deposition is estimated to be substantially reduced in future projections, and resulting total soluble iron deposition in the future may also markedly decrease owing to its probably large contribution (about 60% in our estimate) to the atmospheric soluble iron deposition at present day. Meeting the ambitious target to achieve global carbon neutrality by cutting consumption of fossil fuels in the coming decades would substantially reduce the anthropogenic emissions. Comprehensive analysis of the impacts of reducing iron availability from AN sources on net primary production are required in the context of future changes in ocean mixed-layer depths by atmospheric warming³⁷. It is also important to further explore the iron-climate feedbacks in the Earth system under a changing climate⁵. We suggest ocean biogeochemical models and earth system models fully considering the role of AN sources in the atmospheric soluble iron inputs to the Southern Ocean based on this study.

METHODS

Global aerosol model simulations

We conducted global aerosol simulations using the Community Atmosphere Model version 5 (CAM5)³⁸ with the Aerosol Two-dimensional bin module for foRmation and Aging Simulation version 2 (CAM-ATRAS)^{39–41} with modifications for iron particles. We added four iron minerals, derived

from anthropogenic sources, to the model, namely magnetite, hematite, illite, and kaolinite, along with a biomass burning (BB) iron. All aerosol components were assumed to be internally mixed, and resolved into 12 particle size bins from 1 to 10,000 nm in diameter. The CAM-ATRAS model considers emissions, gas-phase chemistry, new particle formation, condensation/coagulation, aerosol activation, dry/wet deposition, and aerosol interactions with radiation and clouds. We have improved the aerosol in-cloud wet scavenging processes for mixed-phase clouds, which have been demonstrated, by the validation with many aircraft measurements of black carbon concentrations, to result in a more reasonable spatial distribution of black carbon concentrations over high-latitude regions⁴².

The model was run using a horizontal resolution of $1.9^\circ \times 2.5^\circ$ (latitude \times longitude) with 30 vertical layers from the surface to ~ 40 km. In our simulations, global monthly anthropogenic emissions of aerosols and reactive gases in 2010 (present day) were taken from Hoesly et al.⁴³, based on the Community Emissions Data System. Daily BB emissions of aerosols and tracer gases were taken from the Global Fire Emissions Database version 4⁴⁴. Dust emission fluxes were calculated online using the scheme of Zender et al.⁴⁵, with modifications by Albani et al.⁴⁶ and size distributions of Kok⁴⁷. The meteorological fields were nudged by using the Modern-Era Retrospective analysis for Research and Applications Version 2 data. All simulations in this study were run with present-day climatological data for sea surface temperature and sea ice.

Present and future anthropogenic iron emissions

In the control (CTRL) simulation, the anthropogenic iron emission inventory developed by Rathod et al.²⁵ was used to model global-scale atmospheric iron concentrations. The inventory used in the CTRL simulation was developed by using a fuel- and technology- based methodology for calculating combustion iron emissions from residential, transportation, and industrial activities. The CTRL simulation was performed for two time periods, 2008–2011 and 2015–2018; in each case, the results for the last 3 years were used for the comparisons with the atmospheric magnetite measurements over the Southern Ocean. In our simulations, four iron-containing minerals (magnetite, hematite, illite, and kaolinite with iron fractions by mass of 0.73, 0.70, 0.04, and 0.002, respectively) were considered.

The global sums of the anthropogenic iron emissions were 1.6 Tg Fe yr^{-1} as magnetite, 0.52 Tg Fe yr^{-1} as hematite, 0.11 Tg Fe yr^{-1} as illite, and

0.026 Tg Fe yr⁻¹ as kaolinite. Note that the magnetite emission in this new inventory was higher than our previous estimate (1.3 Tg Fe yr⁻¹), which was constrained by limited observations only in the Northern Hemisphere⁸. Magnetite emissions from the Southern Hemisphere (90° S–0°) in our simulations were also higher (0.13 vs. 0.075 Tg Fe yr⁻¹) than the previous one (Supplementary Fig. 1). The magnetite particles in the CTRL simulation had a global mean lifetime of 3.1 days, consistent with that in the simulation by Matsui et al.⁸. Because iron as magnetite has the largest share (~70%) of total anthropogenic iron emissions both globally and over the Southern Hemisphere in the emission inventory, magnetite iron dominated the atmospheric abundance of anthropogenic iron in the CTRL simulation. The modeled global annual mean burdens of iron in the atmosphere as the four anthropogenic iron-bearing minerals, i.e., magnetite, hematite, illite, and kaolinite, were 13, 4.3, 0.82, and 0.20 Gg, respectively.

We find that magnetite concentration profiles in the CTRL simulation are notably underestimated relative to the observations over the Southern Pacific and the high-latitude Southern Ocean. To reduce this gap, we scaled upward the emissions of all four anthropogenic iron minerals by a factor of 5 separately in the Southern Africa, Australia, and Southern America (shown in Supplementary Fig. 3), as magnetite originates from diverse sources²⁴ and probably serves as a proxy of anthropogenic iron budgets in the atmosphere. We find that the scaling of AN iron emissions in the Southern Africa can reduce the observation-simulation discrepancies in most of the Southern Ocean, and thus use this case as a reasonable upper limit of anthropogenic iron budgets over the Southern Ocean (referred to as CTRL_HIGH).

We performed an additional simulation experiment using the anthropogenic iron emission inventory developed by Luo et al.²⁶ (Luo2008), which has been used by many previous studies^{27,48}. Because the Luo2008 inventory did not provide information about iron speciation, anthropogenic iron was treated as a single species in this simulation. The global total anthropogenic iron emissions used in the CTRL and Luo2008 simulations were 2.2 and 0.66 Tg Fe yr⁻¹, respectively. The size distribution of anthropogenic iron emissions in all simulations followed the sized-revolved observations of magnetite based on a power function⁴⁹. It is important to note that the emission sizes of iron-bearing particles affect their long-range transport and lifetimes. Finer-sized iron minerals can be more soluble because they have longer lifetimes and larger potential for iron dissolution¹².

To predict future changes in anthropogenic combustion iron emissions, we scaled the present-day emissions to future conditions based on four Tier-1 shared socio-economic pathways (SSPs) at 2100: SSP1–26, SSP2–45, SSP3–70, and SSP5–85. We first calculated the ratios of projected black carbon emissions from anthropogenic sources for each SSP scenario at 2100 to present-day emissions in each grid cell. Because fossil fuel combustion is one of the major sources of both black carbon and anthropogenic iron emissions, the projected changes in anthropogenic iron from the present day to the future were assumed to be the same as those of black carbon; thus, these grid-resolved ratios of black carbon emissions were used to scale present-day anthropogenic iron emissions from both the Luo2008 inventory²⁶ and the new inventory of Rathod et al.²⁵ to obtain their corresponding future emissions. In this case, the present-to-future ratios of iron emissions from metal smelting for the new inventory was not explicitly calculated and simply assumed as the same with those from fossil fuel combustion. By considering four different future scenarios, we were able to explore the possible ranges of future changes in anthropogenic iron emissions.

Combustion iron emissions from open biomass burning were calculated based on Luo et al.²⁶. The global sum of iron emissions from biomass burning was estimated to be 1.07 Tg Fe yr⁻¹. Dust iron emissions were not treated in our model but we assumed a constant iron content of 3.5% in dust^{5,50,51} for the calculation of atmospheric iron deposition. Estimates of BB and dust iron emission fluxes remain uncertain and may significantly alter the contributions of different sources on soluble iron deposition in the Southern Ocean, as we discussed in Supplementary Note.

Calculation of soluble iron deposition flux

Soluble iron deposition fluxes to the oceans were calculated by multiplying the monthly accumulated deposition flux of iron from each source (anthropogenic combustion, biomass burning, and dust) in each grid cell by the corresponding fractional solubility. The global grid-resolved fractional solubility for iron that is deposited to ocean basins was provided by a newly developed iron processing module in a CAM model that

represented the proton- and the organic ligand-promoted dissolution of iron-bearing minerals¹⁹. In this dataset, the averaged fractional solubility of iron at deposition across all grids in the Southern Ocean (>30°S) (shown in Supplementary Fig. 4) was 7.3%, 16%, and 1.5% for anthropogenic, BB, and dust sources, respectively, which were within a broad range of solubility values reported in previous studies^{48,52–54}. It should be mentioned that these solubilities were used for both present-day and future simulations, though they might change in future conditions due to changes in atmospheric processing^{12,19}. Incorporation of a detailed iron dissolution scheme in our model in future studies will enable us to capture the effects of future anthropogenic non-iron emission changes (e.g., in sulfur dioxide and organics) on the fractional solubility of iron. We also used the same solubility data as the CTRL simulation to estimate soluble iron deposition in the CTRL_HIGH simulation. The related uncertainties are discussed in the Supplemental Note 2.

Comparison with magnetite measurements

A global-scale aircraft measurement dataset of an anthropogenic-sourced iron oxide²³ was used to evaluate the modeled anthropogenic iron budgets in the troposphere. The data comprised the observations from eight series of flight campaigns over the oceans: four series during the High-performance Instrumented Airborne Platform for Environmental Research (HIAPER) Pole-to-Pole Observations (HIPPO 2–5) research campaigns in 2009–2011⁵⁵ and all four of the Atmospheric Tomography Mission (ATOM 1–4) in 2016–2018⁵⁶. These observations were made by using a modified single-particle soot photometer (SP2), and anthropogenic iron-containing particles were identified from the SP2 measurements²³. The SP2 method is most sensitive to magnetite-like particles among all kinds of anthropogenic iron oxides. In the campaign, about 100% of magnetite mass was detected, while other minerals like hematite probably have much lower detection efficiency within the sampling size ranges²³. The recent observations in East Asia have also indicated that the samples of anthropogenic iron oxides observed by the SP2 were in the form of aggregated magnetite nanoparticles^{24,49}. Therefore, we conducted the comparison of modeled anthropogenic magnetite with the observation data. Moreover, because the SP2 used in those campaigns measured iron oxide aerosols in the 180–1290 nm size range (volume equivalent diameter), we compared them only with the modeled magnetite in the size bins between 230 and 1250 nm. We extracted the model results at each time step (30 min) and grid cell along the flight route, and then averaged both the simulation and observation results over specific oceanic regions covered during the eight flight campaigns to generate regional mean vertical profiles of magnetite concentrations. The vertical profiles produced from both simulations and observations were binned at intervals of around 160 hPa because of the low number of particles observed in each campaign. We also compared modeled black carbon concentrations with the measurement datasets from these campaigns. The possible uncertainties in the model-observation comparison of magnetite concentrations were discussed in the Supplemental Note 2.

DATA AVAILABILITY

HIPO and ATOM campaign data can be found at <https://esrl.noaa.gov/csl/groups/csl6/measurements/> and <https://espoarchive.nasa.gov/archive/browse/ATOM>. The global simulation results of atmospheric soluble iron deposition that can be used for ocean biogeochemistry modeling are publicly available at <https://doi.org/10.5281/zenodo.5229867>.

CODE AVAILABILITY

The Community Atmospheric Model version 5 in the frame work of CESM1.2 is freely available at <https://www.cesm.ucar.edu/models/cesm1.2/>. Codes developed for the analysis of the model outputs are available from the corresponding authors upon request.

Received: 9 September 2021; Accepted: 11 March 2022;

Published online: 13 April 2022

REFERENCES

1. Mahowald, N. M. et al. Aerosol trace metal leaching and impacts on marine microorganisms. *Nat. Commun.* **9**, 2614 (2018).

2. de Baar, H. J. W. et al. Synthesis of iron fertilization experiments: from the iron age in the age of enlightenment. *J. Geophys. Res.-Oceans* **110**, C09S16 (2005).
3. Boyd, P. W. et al. Mesoscale iron enrichment experiments 1993-2005: synthesis and future directions. *Science* **315**, 612 (2007).
4. Moore, J. K., Doney, S. C., Glover, D. M. & Fung, I. Y. Iron cycling and nutrient-limitation patterns in surface waters of the World Ocean. *Deep Sea Res. Part II* **49**, 463–507 (2001).
5. Jickells, T. D. et al. Global iron connections between desert dust, ocean biogeochemistry, and climate. *Science* **308**, 67 (2005).
6. Jickells, T. & Moore, C. M. The importance of atmospheric deposition for ocean productivity. *Annu. Rev. Ecol. Evol. Syst.* **46**, 481–501 (2015).
7. Tagliabue, A. et al. The integral role of iron in ocean biogeochemistry. *Nature* **543**, 51–59 (2017).
8. Matsui, H. et al. Anthropogenic combustion iron as a complex climate forcer. *Nat. Commun.* **9**, 1593 (2018).
9. Ito, A. et al. Pyrogenic iron: The missing link to high iron solubility in aerosols. *Sci. Adv.* **5**, eaau7671 (2019).
10. Pinedo-González, P. et al. Anthropogenic Asian aerosols provide Fe to the North Pacific Ocean. *Proc. Natl Acad. Sci. USA* **117**, 27862 (2020).
11. Conway, T. M. et al. Tracing and constraining anthropogenic aerosol iron fluxes to the North Atlantic Ocean using iron isotopes. *Nat. Commun.* **10**, 2628 (2019).
12. Hamilton, D. S. et al. Recent (1980 to 2015) trends and variability in daily-to-interannual soluble iron deposition from dust, fire, and anthropogenic sources. *Geophys. Res. Lett.* **47**, e2020GL089688 (2020).
13. Martin, J. H. Glacial-interglacial CO₂ change: the iron hypothesis. *Paleoceanography* **5**, 1–13 (1990).
14. Martin, J. H., Gordon, M. & Fitzwater, S. E. The case for iron. *Limnol. Oceanogr.* **36**, 1793–1802 (1991).
15. Marinov, I., Gnanadesikan, A., Toggweiler, J. R. & Sarmiento, J. L. The Southern Ocean biogeochemical divide. *Nature* **441**, 964–967 (2006).
16. Watson, A. J., Bakker, D. C. E., Ridgwell, A. J., Boyd, P. W. & Law, C. S. Effect of iron supply on Southern Ocean CO₂ uptake and implications for glacial atmospheric CO₂. *Nature* **407**, 730–733 (2000).
17. Moore, C. M. et al. Processes and patterns of oceanic nutrient limitation. *Nat. Geosci.* **6**, 701–710 (2013).
18. Hamilton, D. S. et al. Impact of changes to the atmospheric soluble iron deposition flux on ocean biogeochemical cycles in the anthropocene. *Glob. Biogeochem. Cycles* **34**, e2019GB006448 (2020).
19. Hamilton, D. S. et al. Improved methodologies for Earth system modelling of atmospheric soluble iron and observation comparisons using the Mechanism of Intermediate complexity for Modelling Iron (MIMI v1.0). *Geosci. Model Dev.* **12**, 3835–3862 (2019).
20. Ito, A. Atmospheric processing of combustion aerosols as a source of bioavailable iron. *Environ. Sci. Technol. Lett.* **2**, 70–75 (2015).
21. Boyd, P. W. & Ellwood, M. J. The biogeochemical cycle of iron in the ocean. *Nat. Geosci.* **3**, 675–682 (2010).
22. Ito, A., Ye, Y., Baldo, C. & Shi, Z. Ocean fertilization by pyrogenic aerosol iron. *npj Clim. Atmos. Sci.* **4**, 30 (2021).
23. Lamb, K. D. et al. Global-scale constraints on light-absorbing anthropogenic iron oxide aerosols. *npj Clim. Atmos. Sci.* **4**, 15 (2021).
24. Yoshida, A. et al. Abundances and microphysical properties of light-absorbing iron oxide and black carbon aerosols over East Asia and the Arctic. *J. Geophys. Res.-Atmos* **125**, e2019JD032301 (2020).
25. Rathod, S. D. et al. A mineralogy-based anthropogenic combustion-iron emission inventory. *J. Geophys. Res.-Atmos.* **125**, e2019JD032114 (2020).
26. Luo, C. et al. Combustion iron distribution and deposition. *Glob. Biogeochem. Cycles* **22**, GB1012 (2008).
27. Myriokefalitakis, S. et al. Changes in dissolved iron deposition to the oceans driven by human activity: a 3-D global modelling study. *Biogeosciences* **12**, 3973–3992 (2015).
28. Scanza, R. A. et al. Atmospheric processing of iron in mineral and combustion aerosols: development of an intermediate-complexity mechanism suitable for Earth system models. *Atmos. Chem. Phys.* **18**, 14175–14196 (2018).
29. Guieu, C. et al. The significance of the episodic nature of atmospheric deposition to low nutrient low chlorophyll regions. *Glob. Biogeochem. Cycles* **28**, 1179–1198 (2014).
30. Kok, J. F., Ward, D. S., Mahowald, N. M. & Evan, A. T. Global and regional importance of the direct dust-climate feedback. *Nat. Commun.* **9**, 241 (2018).
31. Feng, L. et al. The generation of gridded emissions data for CMIP6. *Geosci. Model Dev.* **13**, 461–482 (2020).
32. Ward, D. S. et al. The changing radiative forcing of fires: global model estimates for past, present and future. *Atmos. Chem. Phys.* **12**, 10857–10886 (2012).
33. Pechony, O. & Shindell, D. T. Driving forces of global wildfires over the past millennium and the forthcoming century. *Proc. Natl Acad. Sci. USA* **107**, 19167 (2010).
34. Ito, A. et al. Evaluation of aerosol iron solubility over Australian coastal regions based on inverse modeling: implications of bushfires on bioaccessible iron concentrations in the Southern Hemisphere. *Prog. Earth Planet. Sci.* **7**, 42 (2020).
35. Tang, W. et al. Widespread phytoplankton blooms triggered by 2019–2020 Australian wildfires. *Nature* **597**, 370–375 (2021).
36. Hutchins, D. A. & Boyd, P. W. Marine phytoplankton and the changing ocean iron cycle. *Nat. Clim. Change* **6**, 1072–1079 (2016).
37. Llorc, J., Lévy, M., Sallée, J. B. & Tagliabue, A. Nonmonotonic response of primary production and export to changes in mixed-layer depth in the Southern Ocean. *Geophys. Res. Lett.* **46**, 3368–3377 (2019).
38. Liu, X. et al. Toward a minimal representation of aerosols in climate models: description and evaluation in the community atmosphere model CAM5. *Geosci. Model Dev.* **5**, 709–739 (2012).
39. Matsui, H. Development of a global aerosol model using a two-dimensional sectional method: 1. Model design. *J. Adv. Model. Earth Syst.* **9**, 1921–1947 (2017).
40. Matsui, H. & Mahowald, N. Development of a global aerosol model using a two-dimensional sectional method: 2. Evaluation and sensitivity simulations. *J. Adv. Model. Earth Syst.* **9**, 1887–1920 (2017).
41. Matsui, H., Koike, M., Kondo, Y., Fast, J. D. & Takigawa, M. Development of an aerosol microphysical module: aerosol Two-dimensional bin module for foRmation and Aging Simulation (ATRAS). *Atmos. Chem. Phys.* **14**, 10315–10331 (2014).
42. Liu, M. & Matsui, H. Improved simulations of global black carbon distributions by modifying wet scavenging processes in convective and mixed-phase clouds. *J. Geophys. Res. Atmos.* **126**, e2020JD033890 (2021).
43. Hoesly, R. M. et al. Historical (1750–2014) anthropogenic emissions of reactive gases and aerosols from the Community Emissions Data System (CEDS). *Geosci. Model Dev.* **11**, 369–408 (2018).
44. Giglio, L., Randerson, J. T. & van der Werf, G. R. Analysis of daily, monthly, and annual burned area using the fourth-generation global fire emissions database (GFED4). *J. Geophys. Res. Biogeo* **118**, 317–328 (2013).
45. Zender, C. S., Bian, H. & Newman, D. Mineral Dust Entrainment and Deposition (DEAD) model: description and 1990s dust climatology. *J. Geophys. Res. Atmos* **108**, 4416 (2003).
46. Albani, S. et al. Improved dust representation in the Community Atmosphere Model. *J. Adv. Model. Earth Syst.* **6**, 541–570 (2014).
47. Kok, J. F. A scaling theory for the size distribution of emitted dust aerosols suggests climate models underestimate the size of the global dust cycle. *Proc. Natl Acad. Sci. USA* **108**, 1016 (2011).
48. Myriokefalitakis, S. et al. Reviews and syntheses: the GESAMP atmospheric iron deposition model intercomparison study. *Biogeosciences* **15**, 6659–6684 (2018).
49. Moteki, N. et al. Anthropogenic iron oxide aerosols enhance atmospheric heating. *Nat. Commun.* **8**, 15329 (2017).
50. Duce, R. A. & Tindale, N. W. Atmospheric transport of iron and its deposition in the ocean. *Limnol. Oceanogr.* **36**, 1715–1726 (1991).
51. Shi, Z. et al. Impacts on iron solubility in the mineral dust by processes in the source region and the atmosphere: a review. *Aeolian Res* **5**, 21–42 (2012).
52. Guieu, C., Bonnet, S., Wagener, T. & Loÿe-Pilot, M.-D. Biomass burning as a source of dissolved iron to the open ocean? *Geophys. Res. Lett.* **32**, L19608 (2005).
53. Takahashi, Y. et al. Seasonal changes in Fe species and soluble Fe concentration in the atmosphere in the Northwest Pacific region based on the analysis of aerosols collected in Tsukuba, Japan. *Atmos. Chem. Phys.* **13**, 7695–7710 (2013).
54. Baker, A. R. & Jickells, T. D. Mineral particle size as a control on aerosol iron solubility. *Geophys. Res. Lett.* **33**, L17608 (2006).
55. Wofsy, S. C. HIAPER Pole-to-Pole Observations (HIPPO): fine-grained, global-scale measurements of climatically important atmospheric gases and aerosols. *Philos. Trans. R. Soc. A* **369**, 2073–2086 (2011).
56. Wofsy, S. C., and ATom Science Team. ATom: Aircraft Flight Track and Navigational Data. ORNL DAAC, Oak Ridge, Tennessee, USA. <https://doi.org/10.3334/ORNLDAA/1613> (2018).

ACKNOWLEDGEMENTS

This work was supported by the Ministry of Education, Culture, Sports, Science, and Technology and the Japan Society for the Promotion of Science (MEXT/JSPS) KAKENHI Grant Numbers JP17H04709, JP19H04253, JP19H05699, JP19KK0265, JP20H00196, and JP20H00638, by the MEXT Arctic Challenge for Sustainability phase II (ArCS-II; JPMXD1420318865) project, and by the Environment Research and Technology Development (JPMEERF20202003) of the Environmental Restoration and Conservation Agency of Japan. This work was also supported by the Foundation of Kinoshita Memorial Enterprise (Basic Science Fund) and Nagoya University Research Fund. DSH and NMM acknowledge the assistance of DOE support (DE-SC0006791 and DE-SC0021302). SDR was supported by DOE support (DE-SC0016362) Collaborative Proposal “Fire, Dust, Air, and Water: Improving Aerosol Biogeochemistry Interactions in ACME. The SP2 aircraft data were obtained and analyzed with the support of the NASA Radiation Sciences Program, the NASA Upper Atmosphere

Research Program, and the NOAA Atmospheric Composition and Climate Program. Model simulations were conducted using the Fujitsu PRIMERGY CX400M1/CX2550M5 (Oakbridge-CX) in the Information Technology Center, The University of Tokyo.

AUTHOR CONTRIBUTIONS

H.M. designed the research. M.L. performed model simulations, analyzed the data, and wrote the manuscript. M.L., H.M., D.S.H., S.D.R., K.D.L., J.P.S. and N.M.M. interpreted the results and discussed their implications. All authors commented on and contributed to the manuscript.

COMPETING INTERESTS

The authors declare no competing interests.

ADDITIONAL INFORMATION

Supplementary information The online version contains supplementary material available at <https://doi.org/10.1038/s41612-022-00250-w>.

Correspondence and requests for materials should be addressed to Mingxu Liu or Hitoshi Matsui.

Reprints and permission information is available at <http://www.nature.com/reprints>

Publisher's note Springer Nature remains neutral with regard to jurisdictional claims in published maps and institutional affiliations.



Open Access This article is licensed under a Creative Commons Attribution 4.0 International License, which permits use, sharing, adaptation, distribution and reproduction in any medium or format, as long as you give appropriate credit to the original author(s) and the source, provide a link to the Creative Commons license, and indicate if changes were made. The images or other third party material in this article are included in the article's Creative Commons license, unless indicated otherwise in a credit line to the material. If material is not included in the article's Creative Commons license and your intended use is not permitted by statutory regulation or exceeds the permitted use, you will need to obtain permission directly from the copyright holder. To view a copy of this license, visit <http://creativecommons.org/licenses/by/4.0/>.

© The Author(s) 2022